ACS EARTH AND SPACE CHEMISTRY

http://pubs.acs.org/journal/aesccq

Article

Dust-Catalyzed Oxidative Polymerization of Catechol and Its Impacts on Ice Nucleation Efficiency and Optical Properties

Nicole Link, Nicole Removski, Jingwei Yun, Lauren T. Fleming, Sergey A. Nizkorodov, Allan K. Bertram, and Hind A. Al-Abadleh*

Cite This: *ACS Earth Space Chem.* 2020, 4, 1127−1139

Read Online

ACCESS | Metrics & More | Article Recommendations | Supporting Information

ABSTRACT: Dust is the major source of iron in atmospheric aerosols but little is known about its role in catalyzing polymerization reactions of organics in particles. Using Arizona Test Dust (AZTD) and hematite nanoparticles as laboratory standards and proxies for hematite-rich natural dust, respectively, we show that their reactions with catechol in aqueous slurries lead to the formation of black polycatechol. This observation is in contrast to oxalate and sulfate which form surface complexes promoting the dissolution of iron from the dust particles. Results from ultraviolet−visible spectroscopy and microscopy/elemental mapping show that the formation of polycatechol changed the optical properties of the dust particles and surface chemical composition. Results from ice nucleation studies using a droplet freezing technique show that polycatechol did not significantly impact ice nucleation or block ice nucleation sites on AZTD. In contrast, increasing pH decreased the ice nucleation ability of AZTD. These results highlight the complexity of iron's role in aerosol aging processes, brown carbon formation, and ice nucleation.

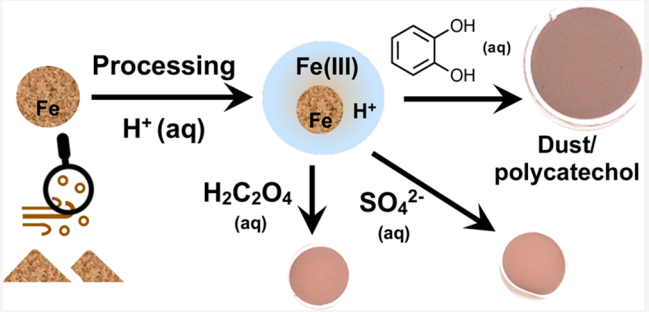

KEYWORDS: *Arizona Test Dust, Hematite Nanoparticles, Iron Minerals Dissolution, Iron Complexes, Polyphenols, Surface Chemical Composition, Surface Charge, Brown Carbon*

INTRODUCTION

Mineral dust from natural and anthropogenic sources is a major component of primary aerosols in the atmosphere with estimated atmospheric loading and emission flux of 19.2 Tg and 1840 Tg yr^{-1}, respectivley.[1,2] The residence time of dust in the atmosphere during long-range transport impacts the climate through affecting surface temperature, wind, cloud formation and lifetime, and precipitation rates.[3] Dust particles also provide surfaces for a range of chemical reactions with trace inorganic and organic species resulting in a change in the chemical composition and hygroscopic properties of these particles.[1,4−6] For example, Asian dust[7−9] and Saharan African dust[10−13] have been shown to undergo extensive processing during long-range transport which impacts their mixing state and morphology.[14] The uptake coefficients of OH, HO_2, H_2O_2, O_3, HCHO, HONO, NO_3, and N_2O_5 on mineral dust particles and their proxies range from 10^{-6} to 0.2.[15] Heterogeneous reactions of African mineral dust with volatile organic compounds (VOCs) were found to be irreversible for limonene and reversible for toluene.[16] Surface reactions of dust with nitric and sulfuric acid were found to lead to the formation of adsorbed nitrate and sulfate, which is enhanced in the presence of water.[4] Photolysis of surface nitrate was reported to release NO_2, which reacts with mineral dust to produce HONO.[4,17]

Mineral dust particles can act as nuclei for ice formation through several different modes including deposition, contact, and condensation or immersion freezing.[1] Several laboratory studies investigated the effect of chemical aging on the ice nucleation (IN) activity of mineral dust including clays such as Arizona test dust (AZTD), illite, kaolinite, montmorillonite, and feldspars.[1,18,19] Here, we focus on previous studies of AZTD in the immersion mode, since they are most relevant for the current work. It was reported that H_2SO_4 coatings could decrease the IN activity compared to fresh particles.[1] Nitric acid coatings on AZTD particles had either a reduction or no effect on the IN activity compared with fresh particles.[20−23] Ammonium salts enhanced the IN ability of AZTD in the immersion freezing mode at low concentrations[24] but could decrease the IN ability at high concentrations.[21,25] Aging of AZTD in acidic or salt solutions and exposure to heat, peroxide, or protease enzyme degraded the IN ability of AZTD in the immersion freezing.[26] No previous studies have

Received: April 22, 2020
Revised: June 4, 2020
Accepted: June 8, 2020
Published: June 8, 2020

investigated the effect of organic coatings on the IN activity of AZTD in the immersion mode, although there have been some studies that showed organic coatings had no effect on the IN activity of Saharan dust and Asian dust in the immersion freezing mode.[27] Despite the recent progress in this area of research, our understanding of the effect of organic coatings on IN ability of mineral dust is far from complete, especially at a molecular level.

Dust particles often dominate aerosol optical density because of their large atmospheric burden and high mass scattering efficiency.[28] They weakly absorb visible radiation: single scattering albedo (SSA) of dust particles is typically in excess of 0.95 at the peak of the solar spectrum[29,30] but it depends on the particle size and mineralogy. Previous field measurements showed that volatile aerosols efficiently transferred from accumulation mode particles onto dust particles in Asian outflows,[31] thus creating an environment for possible reactions between volatile components and dust surfaces. Internal mixing of dust particles with strongly light-absorbing black carbon has been shown to decrease SSA of smaller dust particles,[32] and it can be assumed that strongly light-absorbing organic compounds (i.e., brown carbon) residing on dust particles will have a similar effect on SSA. Because of the high sensitivity of the climate forcing to the optical properties of dust particles,[33] any chemical process that increases light absorption by dust has direct climate relevance.

Dust is a major source of iron in atmospheric aerosols.[34−36] Anthropogenic[37] and biomass burning dust emissions[38,39] are found to contribute 50% of the total iron deposited on the ocean surface.[40−42] Single particle analysis of field-collected aerosols from marine, urban, and rural sites showed that they contain soluble and insoluble iron.[43−54] Field studies reported transport of transition metals, including iron, from the oceans to the atmosphere in the form of sea spray and metal enrichment at the interface of marine aerosols.[55−57] Depending on the source region, the iron mineralogical composition varies from poorly crystalline to crystalline iron oxides to clay minerals.[58] The ratio of crystalline hematite to the total hematite and goethite in dust particles is reported to vary with the geographical location. For example, for Asian dust the ratio ranges from 0.32 to 0.37, whereas for North African dust it ranges from 0.29 to 0.63.[58] As mentioned above, these dust particles undergo atmospheric processing during long-range transport which increases the solubility of iron. Surface area was found to be the predominant factor affecting iron solubility through acidic surface reactions.[59] Mixing with biomass burning products that include gases and aerosols also occurs during long-range transport of dust. For example, Paris et al.[60] reported that entrainment of dust deposited on vegetation makes biomass burning a significant indirect source of iron, whereas mixing with biomass burning aerosols enhances the solubility of iron. Electron microscopy images of aged sulfur-rich dust from Li et al.[8,9] showed that dust particles are encapsulated with an organic film from either primary or secondary sources. In the same studies, soot particles were found to be internally mixed with sulfur-rich and iron-rich particles. This internal mixing promotes iron-catalyzed reactions within or at the surface of dust particles. The speciation (e.g., soluble vs insoluble) and cycling of iron between oxidation states +3 and +2 depends on a number of chemical processes that include absorption efficiency of ultraviolet−visible light, complexation strength to organic matter and inorganic ligands, and dissolution rates of dust.[61−63] The main two mechanisms that lead to iron release from dust and iron (oxyhydr)oxides are proton- and ligand-promoted dissolution.[64−66] Laboratory and field studies from nearly four decades of research into these mechanisms have shown that a number of variables play a role, namely pH, particle size, degree of crystallinity, presence of solar radiation, and structure of Fe-organic surface complexes.[67−70] In general, the highest rates of dissolution occur under acidic conditions[59,71] (pH < 4) in the presence of solar radiation and oxalate with amorphous iron-containing nanoparticles.

Acidic reaction conditions are commonly found in atmospheric aerosol particles, as well as in fog and cloud droplets, where soluble and insoluble iron species catalyze a number of chemical processes.[72−74] Near neutral pH was also reported for cloud droplets.[75] Freshly emitted dust particles contain more than one monolayer of adsorbed water over a wide relative humidity range.[1] There have been no attempts to directly measure the pH of surface water in dust. Basic pH is typically measured in the slurries of unprocessed dust due to the presence of metals that act as Lewis acid sites.[76] The presence of iron in aerosols can influence their oxidative potential through Fenton and photo-Fenton chemistry. The term "oxidative potential" refers to metal-driven redox chemical reactions that lead to the formation of reactive oxygen species such as hydroxyl radicals and hydrogen peroxide.[77] The redox reactions catalyzed by iron can cause not only degradation of water-soluble organics but also formation of soluble and insoluble secondary and high molecular weight organics depending on the chemical structure of the organic precursors. For instance, the formation of soluble organosulfates was reported from the reaction of C2−C4 unsaturated carbonyl compounds methacrolein (MACR) and methyl vinyl ketone (MVK) with bisulfite anion in the presence of Fe(III).[78] On the other hand, reactions of soluble Fe(III) with aromatic compounds detected in biomass burning aerosols and unsaturated C4−C6 dicarboxylic acids detected in aged secondary organic aerosols led to efficient formation of insoluble and colored polymeric compounds, even in the presence of competing ligands such as sulfate and oxalate.[79−82]

While results from the above studies are useful for understanding and predicting the chemical reactivity of dust aerosols, the role of dust in catalyzing polymerization reactions of organics due to the soluble iron fraction, and the effect of dust aging on optical properties and ice nucleation efficiency was not investigated under atmospherically relevant conditions. The hypothesis for the research presented here is that oligomerization reactions of phenolic compounds can take place at the surface of natural dust due to the presence of transition metals such as Fe and the formed oligomers can decrease the IN ability of natural dust. These oligomerization reactions might be as efficient as those producing brown carbon from VOCs precursors.[83] Here, we use Arizona Test Dust (AZTD) as a standard material for laboratory investigations, and hematite nanoparticles as relatively major components of crystalline iron oxides in natural mineral dust from different regions.

MATERIALS AND METHODS

Chemicals. AZTD was purchased from Powder Technology, Inc. and had 0−3 μm nominal particle size, 3.6 ± 0.2% (w/w) Fe, 26 ± 1 m^2 g^{-1} Brunauer−Emmett−Teller (BET) surface area, and was composed of muscovite (33.4%), quartz (30.7%), albite (10.9%), kaolinite (9.1%), sanidine (7.8%), and

https://dx.doi.org/10.1021/acsearthspacechem.0c00107
ACS Earth Space Chem. 2020, 4, 1127−1139

calcite (5.4%) as determined using powder X-ray diffraction. Hematite nanoparticles (HEM) were obtained from U.S. Research Nanomaterials, Inc., contained ≥98% α-Fe_2O_3, and had a nominal particle size of 20−40 nm with 48 ± 5 m^2 g^{-1} BET surface area. The HEM particle size range was obtained for dry particles from high-resolution TEM images that can resolve the boundaries of individual particles.

Other chemicals included 1,2-benzendiol (catechol, C, >99%, CAS 120-80-9, Sigma-Aldrich), oxalic acid dihydrate (≥99%, Ox, CAS 6153-56-6, ACS reagent, Sigma-Aldrich), ammonium sulfate (ACS grade, AS, CAS 7783-20-2, EMD Chemicals), hydrochloric acid (HCl 6 N, Ricca Chemical Company), iron(III) chloride hexahydrate ($FeCl_3 \cdot 6H_2O$, CAS 10025-77-1, Sigma-Aldrich), and sodium hydroxide (NaOH pellets, 99−100%, EMD). Aqueous slurries were prepared using ultrapure Milli-Q water (18.5 MΩ cm). Polycatechol was prepared as described in our earlier publication.[84] Briefly, 2 mL of 102 mM $FeCl_3$ was added to 100 mL of 1 mM catechol at pH 3. The resulting iron to catechol molar ratio after mixing was 2:1. The reaction was allowed to continue in the dark for 2 h followed by filtration on a nylon membrane filter (0.2 μm pore size, 47 mm dia., EMD). After filtration, the products were air-dried overnight. The filters were weighed before and after filtration to measure the mass of the product. Polycatechol (BET surface area 4 ± 0.6 m^2 g^{-1}) could be easily peeled from the filter and kept in a clean vial until further use. Specific surface area values reported for AZTD, HEM, and polycatechol particles were measured by the BET surface area method using N_2 gas in a Nova 2200e multigas surface area analyzer (Quantachrome Instruments).

Acid-Promoted Dissolution Experiments. Acid-promoted dissolution experiments were performed using AZTD. Oxalic acid and ammonium sulfate were added to 10 mL of AZTD slurries (1 g L^{-1}) with and without catechol at pH 1.2 ± 0.1 to test the effect of competing ligands on acid-promoted dissolution. The final concentration of each ligand in these vials was 1 mM. The pH of the slurries containing AZTD with and without catechol and oxalic acid and ammonium sulfate was measured using a calibrated gel-filled or glass pH electrode (Orion). The vials were wrapped in Al foil and left under continuous stirring for 14 days. Digital photographs were taken as a function of time during the experiment to record the color of the slurries. The pH remained around 1.2 ± 0.1 for the duration of the experiment. Then, the slurries were filtered using nylon membrane filters (0.2 μm pore size, 25 mm diameter, EMD). The filters were left to dry overnight at room temperature before a photograph was taken to show qualitative changes in the optical properties of the dust particles. The filtrate solutions were analyzed for dissolved iron as described below.

For comparison with AZTD, acid-promoted dissolution experiments were conducted using 0.3 g L^{-1} HEM slurries (10 mL total volume). Oxalic acid and ammonium sulfate were added to vials with and without catechol at pH 1.1 ± 0.1. The final concentration of each ligand in these vials was 100 μM. The vials were wrapped in Al foil and left under continuous mixing on a flat-top shaker for 16 days. The pH remained around 1.1 ± 0.1 during the reaction time. Then, 1 mL was transferred from each slurry into a clean vial to be used in the STEM/EDS experiments, as described below. The remainders of the slurries were filtered using nylon membrane filters, which were left to dry overnight at room temperature before a photograph was taken. The filtrate solutions were analyzed for dissolved iron as described below.

Spectroscopy Experiments. Ultraviolet−visible (UV−vis) spectra of diluted control and reacted AZTD slurries were collected using a UV−vis spectrophotometer (Ocean Optics USB 4000) in a 1 cm quartz cuvette. Because of the presence of suspended particles in solution, both light scattering and absorption contributed to the recorded spectra. Hence, mass-normalized extinction coefficient (MEC) was calculated in the wavelength range 300−900 nm according to eq 1

$$\mathrm{MEC}(\lambda)\ (\mathrm{cm^2 g^{-1}}) = \frac{\ln(10) \times \text{measured decadic extinction}(\lambda)}{\text{mass concentration of AZTD in slurry } (\mathrm{g\ cm^{-3}}) \times \text{path length (cm)}} \quad (1)$$

Electron Microscopy Experiments. For the scanning transmission electron microscopy coupled with energy dispersive spectroscopy (STEM/EDS) analysis, the samples were spread on silicon nitride window grids from Norcada. Slurries were diluted with a 50 vol % ethanol−water mixture to lessen the degree of particle aggregation on the grids. The experiments were performed with a Joel 2010F field emission gun (FEG) operated at 200 kV. The microscope was equipped with an Oxford Inca EDS system for elemental mapping of iron, oxygen, and carbon. Over 20 images were collected for different particles deposited on multiple grids to ensure that images shown here are representative of the source slurries. For the quantification of the elements in the EDS maps, the software was carefully calibrated with standard samples.

Dissolved Iron Analysis. These experiments were conducted to quantify the concentration of total dissolved iron (DFe) from the acid-promoted dissolution experiments of AZTD and HEM at the end of the acidification process (i.e., 14 days). The slurries were filtered using nylon membrane filters (0.2 μm pore size, 25 mm dia., EMD) as mentioned above. Values of DFe were obtained using Collision/Reaction Cell ICP-MS according to a modified EPA 6020A method[85] by ALS Environmental Laboratories. Briefly, the samples were digested with nitric and hydrochloric acids followed by filtration. These measurements quantified total soluble Fe using standard solutions of acid-digested iron powder. A calibration curve of standard iron concentrations covered the range 0.5−10 mg L^{-1}. Since acid-promoted dissolution of iron-containing materials is a surface process, it is useful to normalize DFe values to the surface area of the particles in the slurries according to eq 2

$$\mathrm{DFe_{SA}} = \frac{[\mathrm{Fe(aq)}]\ (\mathrm{mg\ L^{-1}}) \times \text{volume (L)} \times 10^{-3}\ \mathrm{g\ mg^{-1}}}{\text{amount of hematite in solution (g)} \times \text{specific BET area } (\mathrm{m^2 g^{-1}})} \quad (2)$$

Efficiency of Ice Nucleation Experiments. The effects of pH and reaction time with catechol on the IN efficiency of AZTD particles were tested. The starting pH of solutions in the control and reaction vials containing 1 g L^{-1} AZTD was adjusted to approximately 1, 3, and 7 from the starting pH of ∼9 using HCl. Reaction vials contained 1 mM catechol. The pH and IN efficiency were measured on day 0, 3, 8, and 14. The IN experiments were conducted using the droplet freezing technique, which we used in previously published work.[86] Briefly, 20 droplets (2 μL each) from each control and reaction vial were placed on a hydrophobic glass slide (Hampton Research, Aliso Viejo, CA, U.S.A.), and the slide was placed on the top of a temperature-controlled cooling stage (Grant

https://dx.doi.org/10.1021/acsearthspacechem.0c00107
ACS Earth Space Chem. 2020, 4, 1127−1139

Asymptote). The surface area of AZTD in each droplet was $(5.2 \pm 0.2) \times 10^{-5}$ m^2. The total number of slides was three for each run (i.e., freezing experiment), and hence a total of 60 droplets were analyzed in each freezing experiment. A cover equipped with a digital camera was placed on top of the stage, and nitrogen gas flow started with the stage cooling at a rate of 5 °C min^{-1} until all droplets were frozen as recorded via video. A Matlab script was used to extract values of temperature associated with freezing "events" from video images, which was then used to calculate the "frozen fraction" that corresponds to the percentage of droplets that froze at a given temperature. The temperature that corresponds to 50% frozen fraction is called "T50" and is used as a measure of the ice nucleation efficiency of different samples. The uncertainty in T50 reported here for a given frozen fraction equals the propagated error ($\pm 2\sigma$) that includes the standard deviation from averaging the corresponding values from each slide and the uncertainty in the temperature readout (±0.25 °C). For comparison, experiments were also done using ultrapure water and polycatechol particles (with no AZTD present). Polycatechol was prepared as described above. A slurry of polycatechol in water was prepared to obtain the same surface area of particles similar to that for AZTD slurries, $(5.2 \pm 0.2) \times 10^{-5}$ m^2. This way, each droplet in the freezing experiment of polycatechol had particles with the same surface area as in the experiments with AZTD particles. At the end of the 14 days, STEM and EDS elemental mapping images were recorded for particles from control and reaction slurries. The remaining samples were filtered on nylon membrane filters (0.2 μm pore size, 25 mm dia., EMD) to quantify DFe and take digital images of dry AZTD particles.

Matrix-Assisted Laser Desorption Ionization Time of Flight Mass Spectrometry (MALDI-TOF-MS). These experiments were conducted to obtain data on the structure of polycatechol oligomers using an AB SCIEX TOF/TOF 5800 MALDI System. MALDI is a technique that is commonly used in the analysis of polymer samples.[87] Typically, the sample is mixed with a low molecular weight organic compound (i.e., matrix) that absorbs the laser radiation causing heating, ionization, and desorption of the matrix molecules. Sample molecules also undergo desorption and charge-transfer reactions with matrix ions and are then detected by the TOF-MS. No matrix was needed for the analysis of polycatechol because it absorbs strongly by itself at the wavelength of the laser (337 nm). A concentrated slurry of polycatechol only in methanol was prepared from which samples were spot-deposited on the MALDI stainless steel sample plate forming thin films. The spots were dried in air at room temperature before being loaded to the MALDI-TOF-MS sample holder. Data were acquired in negative ion mode with laser power adjusted to result in the minimum visible damage to the sample. Scans of different spatial domains of the sample were accumulated to ensure reproducibility of mass features.

RESULTS AND DISCUSSION

Dust-Catalyzed Polycatechol Formation as a Function of pH. The reaction of AZTD with dissolved catechol was followed as a function of time and pH in the dark. The reaction conditions at pH 1 and 3 simulate acid-promoted dissolution in atmospheric aerosols (see references in the Introduction). The left and right panels of Figure 1 show photographs of AZTD control (no catechol added) and

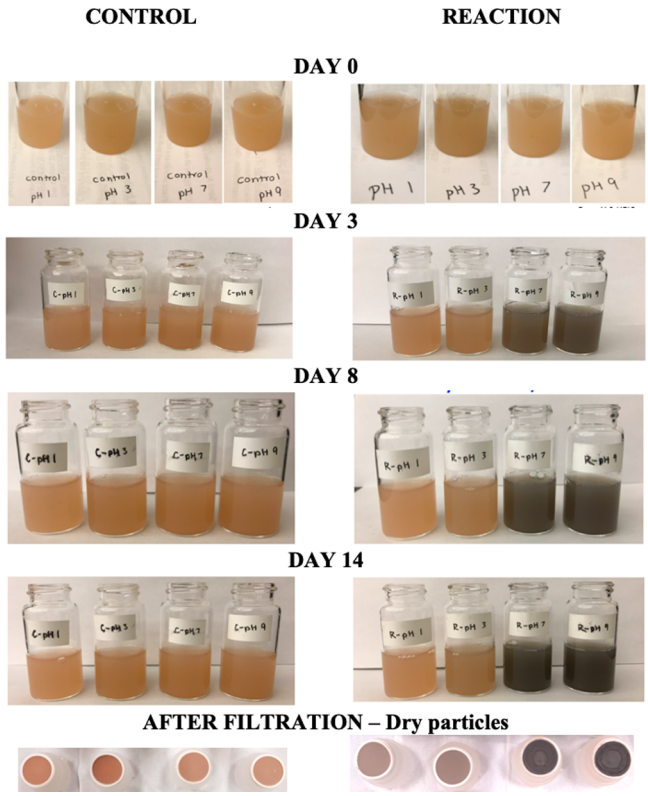

Figure 1. Digital photographs of control (C, left) and reaction (R, right) vials containing AZTD as a function of pH and simulated atmospheric aging time. These samples were used to measure the ice nucleation efficiency of AZTD on each of the stated days as shown in Figure S7. The pH values shown in the label of each vial refers to the starting pH of the slurry. At the end of day 14, the slurries were filtered and the corresponding filters are shown below each vial. The concentration of DFe in the filtrates of C-pH 1, R-pH 1, and R-pH 3 were 9.5, 12.2, and 2.3 mg L^{-1}, respectively. Values of DFe for the other filtrate solutions were below the detection limit of the instrument (0.25 mg L^{-1}).

reaction (with catechol) slurries over a 14 day period and that of the dry particles after filtration. The effect of oxalic acid (Ox) and ammonium sulfate (AS) on the reaction of catechol with AZTD was also investigated at pH 1 (left panels in Figures S1 and S2). Photographs were taken for a qualitative assessment of the color of the particles as a function of time. Photographs of the AZTD slurries in Figures 1, S1, and S2 showed little change in color over the 14 day reaction time. However, the color of the particles on the filters from the reaction vials appeared darker compared to that from the control vials with no catechol. The particles in the AZTD-Cat slurries were also darker than particles in AZTD-Ox and AZTD-AS slurries (Figure S1). The AZTD-Ox-Cat mixtures containing both catechol and the competing oxalate were intermediate in color between the AZTD-Ox and AZTD-Cat slurries (Figure S2) suggesting that the presence of Ox had a suppressing effect on the particle darkening process. The sulfate ligand in AZTD-AS had a smaller effect on the reaction. In Figure S2, the darker color observed for the AZTD-AS-Cat particles on the filter compared with AZTD-Ox-Cat suggests that the reaction kinetics responsible for the darker color is faster in the presence of sulfate than oxalate surface complexes. No filter images on Day 0 were taken because this type of dust aging process takes hours and days, and a filter image for Day 0

https://dx.doi.org/10.1021/acsearthspacechem.0c00107
ACS Earth Space Chem. 2020, 4, 1127−1139

would not have provided further information about the aging process.

Similar studies were conducted using hematite nanoparticles (HEM). The right panel in Figures S1 and S2 shows progressive darkening in the color of the slurry containing hematite nanoparticles and catechol with time (HEM-Cat, HEM-Ox-Cat, and HEM-AS-Cat) compared to those containing only Ox and AS. Particles on the filters after 16 days reaction time also appeared much darker than those in slurries containing no catechol. Previously, we reported that reactions of soluble Fe(III) with catechol and guaiacol led to efficient formation of insoluble and colored polymeric compounds, polycatechol and polyguaiacol, even in the presence of competing ligands such as sulfate and oxalate.[79,81] We also showed that the reaction of soluble Fe(III) in the presence of equimolar amounts of catechol and oxalate was slower in the presence of oxalate leading to the formation of larger polycatechol particles at pH 3. The qualitative results in Figures 1, S1, and S2 with iron-containing materials AZTD and HEM motivated further quantification of the optical properties of slurries and thin films of particles using UV−vis spectroscopy, amounts of dissolved iron, surface composition, and efficiency of ice nucleation of AZTD, as detailed below.

Quantifying Changes in Optical Properties. The reason for the color change observed in Figure 1 was investigated by taking UV−vis transmission spectra for diluted slurries. Figure 2 shows the MEC values for diluted AZTD

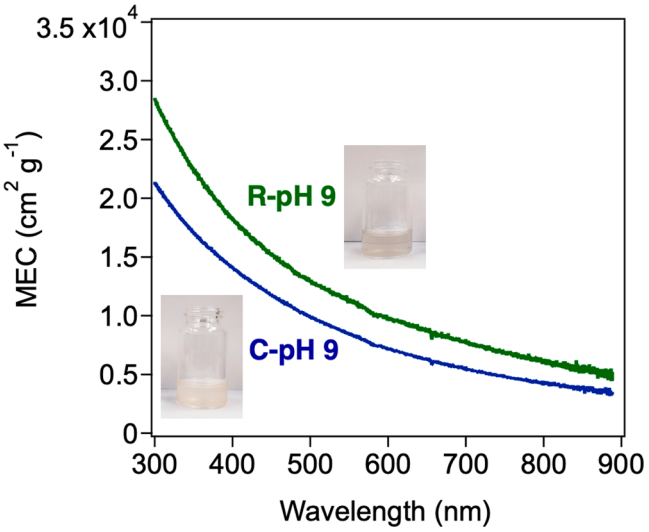

Figure 2. MEC spectra as a function of wavelength for diluted AZTD slurries reacted with catechol at pH 9 (R-pH 9) and control at pH 9 (C-pH 9). For the controls, no catechol was added. The insets show digital photographs of the slurries used in the analysis with mass concentrations of 5.6×10^{-5} g cm^{-3} (R-pH 9) and 1×10^{-4} g cm^{-3} (C-pH 9).

slurries reacted with catechol at pH 9 (R-pH 9) and control at pH 9 (no catechol, C-pH 9). In agreement with the observed darkening of the particles by the reaction, measured MEC values increased in the R-pH 9 sample at all wavelengths. This method cannot separate contributions to the increase in MEC driven by the growth of particles leading to increased scattering and by the deposition of light-absorbing organic material on particles leading to increased absorption. The lack of wavelength-dependent features in the MEC spectrum of the aged samples suggests that the scattering effect dominated the overall extinction.

Quantifying Dissolved Iron. The filtrate solutions from the acid-promoted dissolution experiments at pH 1 with AZTD and HEM in Figures S1 and S2 were analyzed for total DFe using ICP-MS to quantify the effect of ligands on the acid-promoted dissolution of dust and iron oxides. The word "dissolved" used here refers to soluble iron that passed through the pores of the 0.2 μm filter.[88] The dry size of the HEM particles was 20−40 nm based on high-resolution TEM. However, in solution HEM particles readily agglomerate to micrometer size to lower their surface energy. Therefore, filtration through the 0.2 μm pore size filters allows the dissolved fraction or colloids smaller than 200 nm of iron to pass through. Table 1 lists values of DFe for all samples

Table 1. Quantification of Dissolved Iron Using ICP-MS Following Filtration of AZTD and Hematite Samples after 14 d Reaction with Catechol (Cat), Oxalic Acid (Ox), and Ammonium Sulfate (AS) at pH 1

sample	DFe (mg L^{-1})	DFe_{SA} (g m^{-2}) × 100[a]
AZTD-control	30 ± 3	0.12 ± 0.01
AZTD-Cat	20 ± 2	0.08 ± 0.01
AZTD-Ox	22 ± 2	0.09 ± 0.01
AZTD-AS	19 ± 2	0.07 ± 0.01
AZTD-Ox-Cat	23 ± 2	0.09 ± 0.01
AZTD-AS-Cat	22 ± 2	0.09 ± 0.01
HEM-control	12 ± 2	0.09 ± 0.01
HEM-Cat	14 ± 2	0.11 ± 0.01
HEM-Ox	41 ± 4	0.31 ± 0.03
HEM-AS	18 ± 2	0.14 ± 0.01
HEM-Ox-Cat	39 ± 4	0.30 ± 0.03
HEM-AS-Cat	19 ± 2	0.14 ± 0.01

[a]Weight ratio of dissolved Fe (g) per surface area of solid sample (m^2).

studied. Within the uncertainties reported in Table 1, the DFe values show that for AZTD the addition of ligands Cat, Ox, and AS resulted in lower values (average 20 ± 2 mg L^{-1}) compared to the control sample (no ligands, 30 ± 3 mg L^{-1}). Chen and Grassian[64] investigated the reaction of AZTD slurries with oxalic and sulfuric acids at pH 2 over shorter time frames to quantify the amount of dissolved iron. Iron dissolution was found to be higher in the presence of oxalic than sulfuric acid due to the formation of mononuclear bidentate Fe-oxalate complexes. Our findings suggest that the acid-promoted iron dissolution mechanism in AZTD is more important than the ligand-promoted dissolution at pH 1. The pH used in our studies using HCl is lower than that reported by Chen and Grassian where sulfuric, oxalic, and acetic acids at pH 2 and 3 were used, making the ligand-promoted dissolution more important.[64]

In the case of hematite nanoparticles, the presence of Ox nearly tripled the amount of iron released into solution compared to the control (41 ± 4 versus 12 ± 2 mg L^{-1}). The third column in Table 1 lists the ratio of DFe mass relative to the surface area of the solid sample (expressed as DFe_{SA}). The DFe_{SA} values are higher for HEM than AZTD by nearly a factor of 3 for the samples containing oxalate. For example, DFe_{SA} is 0.3 ± 0.03 for HEM-Ox versus 0.09 ± 0.01 for AZTD-Ox. Values of DFe_{SA} using catechol as a ligand were slightly higher for HEM-C compared to AZTD-C (0.11 ± 0.01

https://dx.doi.org/10.1021/acsearthspacechem.0c00107
ACS Earth Space Chem. 2020, 4, 1127−1139

vs 0.08 ± 0.01). DFe_{SA} nearly doubled for HEM-AS compared to AZTD-AS (0.14 ± 0.01 vs 0.07 ± 0.01).

These results suggest that the nanometer-size range of the hematite particles affected the dissolution mechanism to a higher extent than the micron-size AZTD particles for all the ligands studied here with oxalate resulting in the highest DFe_{SA} values. This finding is consistent with previous studies.[64,65] The size dependence likely reflects the impact of the particle surface area/volume ratio in acid processing that can be achieved in a fixed amount of time.[59] Iron (oxyhyr)oxide nanoparticles such as hematite and goethite have exposed reactive surface planes and large density of defect sites.[65,89,90] On the other hand, micron-size AZTD particles consist mainly of crystalline aluminosilicate clay minerals and hence are structurally different from iron (oxyhyr)oxides.[66] The effect of the ligands used here on iron dissolution can be explained by the types of surface complexes they form with iron sites.[64,65] Oxalate forms bidentate mononuclear complexes with surface Fe under acidic conditions, which labilize surface Fe—O bonds and act as an electron bridge leading to the enhanced release of Fe to the solution compared to proton-promoted dissolution.[64] In the case of catechol, the formation of bidentate binuclear complexes[91,92] with surface Fe under acidic conditions does not enhance dissolution of iron compared to proton-promoted dissolution. This result was explained by the unfavorable activation energy associated with the detachment of two metal cations.[93,94] Catechol was found to enhance iron dissolution from hematite particles under neutral to basic conditions.[91] As an oxyanion, sulfate forms monodentate inner-sphere complexes with hematite under acidic conditions,[95] which is considered weaker than the bidentate and bridging adsorption modes,[64,65] and hence a pronounced effect was not observed in our studies compared to proton-promoted dissolution.

The adsorption of catechol from solution on iron oxides has been studied extensively using batch experiments and infrared spectroscopy over relatively short time frames (minutes to hours).[91,92] Some of these studies were conducted as a function of pH and ionic strength. The spectroscopic data were coupled with density functional theory calculations to elucidate the structure of catechol surface complexes. These studies reported that catechol forms a mixture of protonated monodentate mononuclear and bidentate binuclear complexes. The relative amount of each complex is pH-dependent, where the concentration of the monodentate complex increases with decreasing pH.[92] In summary, proton- and ligand-promoted dissolution of iron minerals and metal oxides in the dark is a complex surface process that is affected by the physicochemical properties of the particles and solution conditions.

Mechanism of Surface-Catalyzed Polycatechol Formation. The darker color of the dried filters obtained after 14 d of simulated acid processing shown in Figures 1, S1, and S2 suggests that the adsorption of catechol to iron-containing materials slowly changes the optical properties of the particles. These reactions take place over relatively long periods of time (days) following the formation of the catechol-iron surface complexes discussed above. In the soil chemistry literature, catechol was found to undergo catalytic abiotic oxidation on the surfaces of iron and manganese oxides under basic pH (pH > 8). Colarieti et al.[96] studied this reaction using UV−vis spectroscopy and reported a three-step mechanism for the formation of polycatechol, a high molecular weight and water-insoluble hydroxylated polymer (Scheme 1). Steps 1 and 2 are

Scheme 1. A Three-Step Mechanism for Abiotic Oxidative Polymerization of Catechol on the Surface of Iron Oxide Per Colarieti et al.[96] and Larson and Hufnal Jr.[97a]

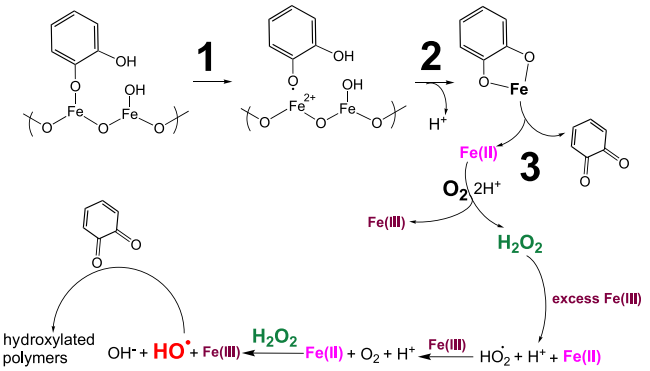

[a]The different colors are used to highlight the oxidation state of the iron in the respective step. The larger size for OH and H_2O_2 is used to highlight the reactive oxygen species generated in the reaction.

heterogeneous reactions, which involve partial oxidation of catechol due to an electron transfer to surface iron and release of Fe(II) to solution. The reduced Fe(II) species in solution further complex to catechol, which undergoes homogeneous oxidation per step 3 in the presence of dissolved oxygen. This reaction step involves cycling between Fe(II) and Fe(III) species and the production of reactive oxygen species, H_2O_2 and OH radicals, as intermediates.[97] As discussed by Colarieti et al.,[96] the basic pH increases the concentration of mono- and bis-complex formation between catechol and Fe(II) in solution and hence speeds up the rate of catechol oxidation and polymerization. In addition, the basic pH in the presence of dissolved oxygen enhances catechol deprotonation and autoxidation to soluble colored products. Larson and Hufnal Jr. studied the effect of pH (5−9.4) on the oxidative polymerization of catechol with soluble metal species using UV−vis spectroscopy.[97] A 10-fold increase in the absorbance at 360 nm (used as the measure for colored polymer formation) was observed at pH 8 compared to pH 7.

Under acidic conditions relevant to atmospheric aerosol pH, Al-Abadleh and co-workers[79,81] reported efficient soluble Fe(III)-catalyzed oxidative polymerization of catechol and guaiacol. Similar experiments were completed with dissolved iron from filtrates of acid dissolution experiments of hematite.[79] Here, we show that this chemistry also takes place over a broad range of pH in the presence of iron-containing dust and iron oxide particles, albeit over days of reaction time. Although the reaction kinetics with AZTD and HEM particles is slower under acidic relative to basic pH per the qualitative assessment of the filter images in Figure 1, polycatechol formation changes the optical properties.

Surface Chemical Composition. Figures 3 and 4 show the STEM images of reacted AZTD and HEM particles. The samples were taken from slurries containing catechol following nearly 2 weeks of reaction at pH 1 (Figures S3 and S4). The STEM images were coupled with EDS elemental mapping to show the distribution of carbon, oxygen, and iron in the samples. The images from control samples (no catechol in solution) are also shown for comparison. Images of AZTD reacted with catechol in the presence of Ox and AS in equimolar amounts are shown in Figure S5. Figure 4 also shows particles from reaction mixtures containing oxalate and

https://dx.doi.org/10.1021/acsearthspacechem.0c00107
ACS Earth Space Chem. 2020, 4, 1127−1139

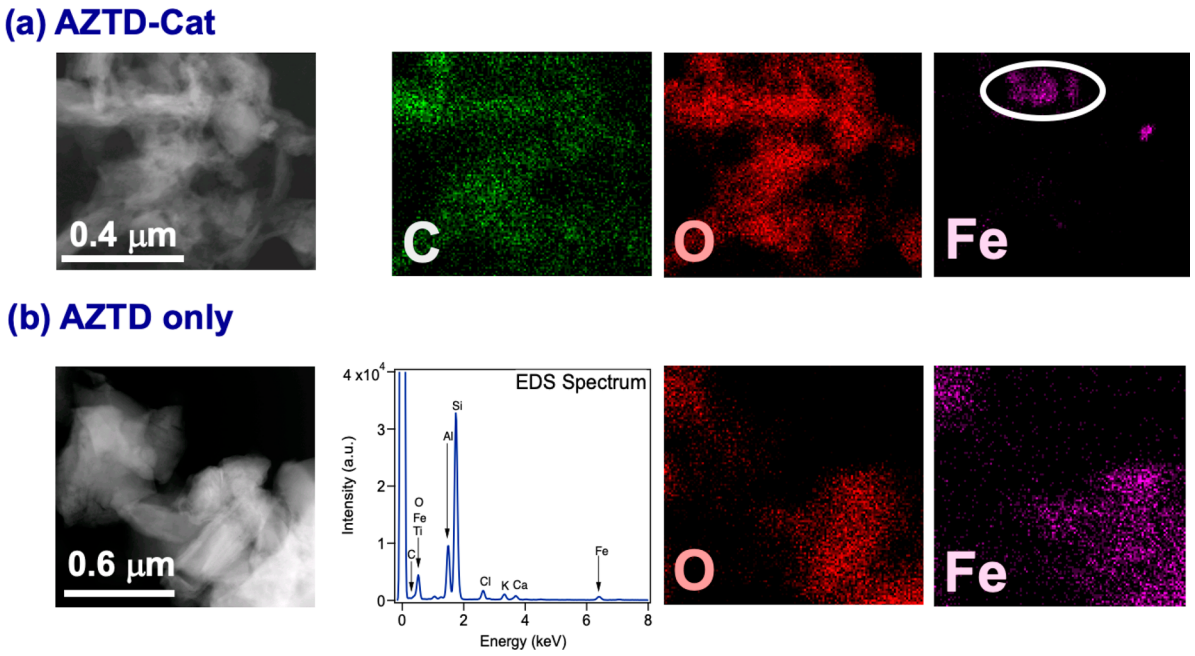

Figure 3. Representative STEM images and EDS elemental mapping of AZTD particles with (a) polycatechol (AZTD-Cat) and (b) control (AZTD only, no catechol in solution). Slurries used for the images are shown in Figure S3. The images labeled C, O, and Fe represent elemental maps for the corresponding atoms. In (b), no carbon signal was detected in the EDS spectrum; hence, no carbon map was generated.

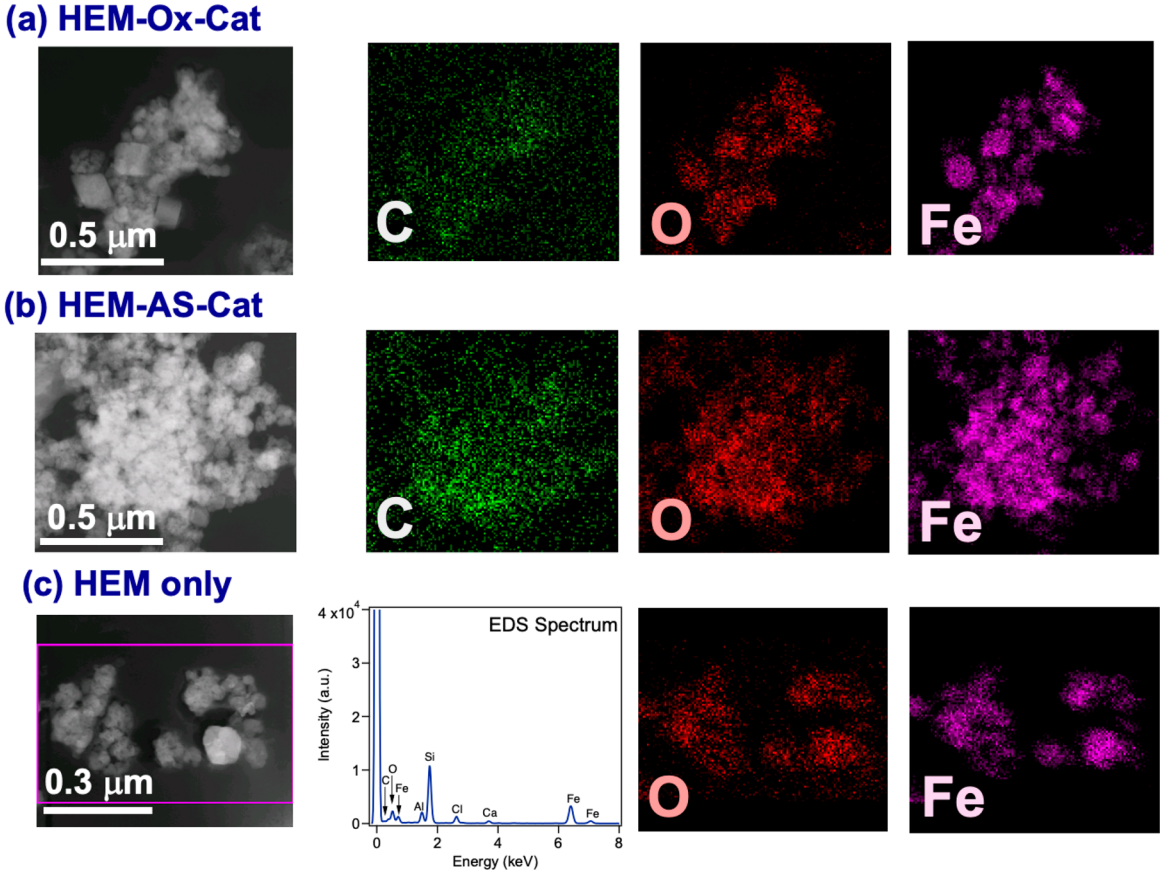

Figure 4. Representative STEM images and elemental mapping of HEM particles with polycatechol, from the reaction of catechol in the presence of Ox (HEM-Ox-Cat), and AS (HEM-AS-Cat) and from control slurries (HEM only, no catechol in solution). Slurries used for the images are shown in Figure S4 in the Supporting Information. The images labeled C, O, and Fe represent elemental maps for the corresponding atoms. No carbon signal was detected in the EDS spectrum; hence, no carbon map was generated.

https://dx.doi.org/10.1021/acsearthspacechem.0c00107
ACS Earth Space Chem. 2020, 4, 1127−1139

ammonium sulfate. Images of dust particles in Figures 3 and S5 show that the iron signals in the elemental maps are concentrated in some areas. In these elemental maps, brighter areas correspond to higher relative amounts than dimmer areas. The carbon signals in Figures 3a and S5 for particles reacted with catechol are not uniformly distributed across the image with some areas having a larger amount of detected carbon than the others.

Table S1 lists the atom % of Fe, O, and C signals. The C atom % is higher for AZTD-Cat at 4.5% compared to 1.9 and 2.4% for AZTD-Ox-Cat and AZTD-AS-Cat. The values for C atom % using HEM nanoparticles are 4.1 and 4.2% for HEM-Ox-Cat and HEM-AS-Cat, respectively. The carbon signal was undetectable for the control AZTD and HEM samples (no catechol). Also, the carbon signal was undetectable for samples with oxalate and AS only (no catechol). Although oxalate contains carbon atoms, the amount oxalate adsorbed to the surface is too low to be detected in the EDS spectra of AZTD and HEM particles reacted with oxalate only (see Figure S6). We can infer that the observable carbon signal in AZTD and HEM particles exposed to catechol comes from polycatechol deposits that are considerably thicker than a monolayer. This polycatechol is responsible for the qualitative darkening of the color of these particles shown in Figures 1, S1, and S2.

Moreover, there is some colocalization in Figures 3a and S5a,b of the iron and the carbon signals suggesting that the iron content in the dust particles might be anchoring the polymeric network of polycatechol, which upon formation, might encapsulate the dust particle. Similar observations can be made from the images in Figure 4 with hematite nanoparticles, where there is clear association of carbon with iron. The presence of oxalate and ammonium sulfate in equimolar amounts to catechol did not suppress polycatechol formation in either AZTD or HEM particles (see photographs of filters in Figures S1 and S2). We reported earlier the effect of oxalate and ammonium sulfate on the efficiency of polycatechol formation from the reaction of catechol with soluble Fe(III) in solution at pH 3.[81] In these aqueous phase experiments, oxalate was found to suppress the mass yield of polycatechol when its concentration was higher than that of catechol. Higher ammonium sulfate to catechol molar ratio had no effect on the mass yield of polycatechol. However, in the experiments with AZTD and HEM reported here over much longer time scales the presence of the competing oxalate and sulfate ligands did not appear to inhibit polycatechol formation. Quantifying the yield of polycatechol in these systems is currently underway.

Structure of Polycatechol. To explore the structure of polycatechol, mass spectra from thin film samples were collected using MALDI-TOF. Figure 5 shows a representative negative ion mode mass spectrum of polycatechol in the m/z range 200−450. Table 2 lists the tentative assignment of the peaks to chemical formulas and structures of oligomeric fragments. While the peak pattern shown in Figure 5 is complex, the highest intensities were associated with the trimer (around m/z 330) and the tetramer species (around m/z 430). Higher order oligomers, above m/z 450, were not reproducibly observed. For comparison, Pillar et al.[99] observed dimers and trimers in the electrospray ionization mass spectra of organic solvent extracts of soluble products from the heterogeneous ozonolysis of catechol thin films. Similar observations were made by Lavi et al.[82] who characterized soluble oligomeric

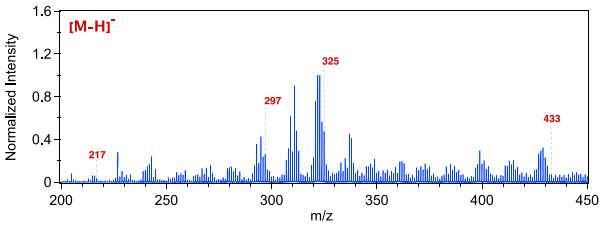

Figure 5. Representative MALDI-TOF mass spectrum of a polycatechol thin film in the negative reflector mode. The assignment of marked fragments is listed in Table 2.

Table 2. Tentatively Identified Oligomeric Hydroxylated Aromatic Species from Polycatechol in the MALDI-TOF Spectrum[a]

Measured [M-H]$^-$ $[C_{6n}O_{2n}H_{10+4(n-2)}\text{-H}]^-$	Proposed structure	Ref.
217 n=2, $[C_{12}O_4H_9]^-$	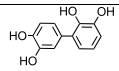	99
325 n=3, $[C_{18}O_6H_{13}]^-$	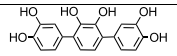	99
433 n=4, $[C_{24}O_8H_{17}]^-$	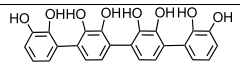	This work
Measured [M-H]$^-$	**Proposed structure**	**Ref.**
297 $[C_{12}O_9H_9]^-$	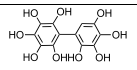	99

[a]The references refer to studies that reported these structures from the oxidation of catechol using mass spectrometry.

products from the reaction of Fe(III) with phenolic compounds that include guaiacol, syringol, and *o*- and *p*-cresol.

Impact of Polycatechol on AZTD Ice Nucleation Efficiency. The effect of pH and reaction with catechol on the IN efficiency of AZTD was studied over a 14 day period in the dark. Figure 1 shows digital images of the slurry samples used in these studies and the dry particles after filtration following 14 days of simulated atmospheric aging. The fraction of droplets frozen from each reaction vial as a function of temperature is shown in Figure S7. The data for ultrapure water only and polycatechol particles (no AZTD) were also collected for comparison. The variation of pH over time is shown in Figure S8 for both reaction and control samples. The pH did not change with time for a starting pH ∼ 1, whereas the pH slightly increased for a starting pH of ∼4. For a starting pH ∼ 7 and 9, the pH of the reaction samples decreased likely due to a combination of the release of protons from the surface reaction with catechol per step 2 in Scheme 1 and an increase of carbonate from the uptake of atmospheric CO_2, which exponentially increases with increasing pH.[98] For a starting pH of ∼9, the pH of the control samples also decreased likely due to an increase of carbonate, as discussed above.

Figure 6 shows T50 values as a function of time and pH for control and reaction vials. At pH 1 and 3, the T50 values for AZTD samples with and without catechol overlap within the uncertainties of the measurements, suggesting no effect of catechol on the ice nucleation efficiency of AZTD. Also, the change in T50 values with time is less than the uncertainty in the measurements. At pH 7, a decrease in T50 was observed at an apparent rate of 0.14 ± 0.02 °C d^{-1} for both ATDZ samples

https://dx.doi.org/10.1021/acsearthspacechem.0c00107
ACS Earth Space Chem. 2020, 4, 1127−1139

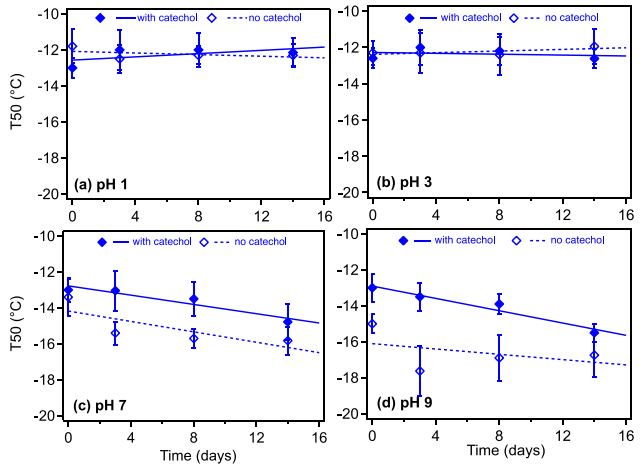

Figure 6. Ice nucleation efficiency as gauged by T50 values as a function of time and starting pH of reaction and control AZTD slurries. Error bars in T50 represent propagated $\pm 2\sigma$. See Materials and Methods for surface area of AZTD in these experiments.

with catechol and ATDZ samples without catechol. At pH 9, a decrease in T50 was observed at an apparent rate of 0.17 ± 0.01 and 0.07 ± 0.03 °C d^{-1} for AZTD samples with and without catechol, respectively, approaching the T50 value obtained for pure polycatechol particles only (see below). At pH 7, which is more atmospherically relevant than pH 9, the T50 for reaction samples was −14.8 ± 1.0 °C after 14 days of simulated atmospheric aging compared to −15.8 ± 0.8 °C for control samples. This small shift in T50 values was likely due to the slightly different pH values for the reaction and control samples (Figure S8).

At pH 7 and 9, the reaction samples containing polycatechol, based on the color of the reaction samples, are compared to the control samples (Figure 1). The lack of a strong effect of polycatechol on T50 values means that polycatechol is either not completely blocking the AZTD surface or polycatechol is also efficient at nucleating ice. To distinguish between these two possible scenarios, experiments were conducted to investigate the ice nucleation efficiency of polycatechol itself in the absence of AZTD particles. The polycatechol slurries (pH unadjusted, ∼6) were prepared to obtain similar surface area as those in the AZTD slurries. The ice nucleation efficiency of polycatechol is shown in the right panel of Figure S7 with a T50 at −17.7 ± 0.8 °C. This T50 value is reproducibly lower than the T50 values for AZTD with polycatechol in all cases. We conclude that polycatechol did not completely block the AZTD surface.

As shown in Figure 6 (empty markers), pH had a statistically significant effect on the ice nucleation efficiency of AZTD in the absence of catechol. After 14 days, for pH 1 and 3 T50 of control samples was about −12 ± 1 °C. The T50 values drop to −15.8 ± 0.8 and −16.7 ± 1.2 °C at pH 7 and 9, respectively. The shift in T50 values of 3.8 ± 1.3 and 4.7 ± 1.6 °C due to more basic pH might be explained by the change in the protonation state of the surface of the minerals identified in AZTD. The points of zero charge (pH_{PZC}) of these minerals are listed in Table S2. These values refer to the pH at which the number of positive sites equal the number of negative sites or the pH at which surface is dominated by neutral sites.[100] The shift in pH from 1 to 9 in our experiments will change the surface charge of AZTD from positive to negative, which may impact the freezing efficiency.[101] The impairment of freezing efficiency of AZTD at basic conditions can be expected, since studies[102,103] have shown that the freezing efficiency of potassium-rich feldspar and quartz was suppressed at alkaline conditions, and feldspars and quartz make up a significant portion (nearly 50% in total) of the AZTD samples investigated.

CONCLUSIONS

We showed that the reaction of catechol with iron in AZTD and hematite particles leads to the formation of black-colored polycatechol over a wide pH range including acidic conditions found in atmospheric aerosol particles. The formation of this colored polymer changed the optical properties of the particles and surface chemical composition. The presence of polycatechol, which was observed under acidic and basic pH conditions, did not cause a significant shift in the ice nucleation efficiency of AZTD. Increasing pH in slurries containing AZTD only (no catechol) was found to lower the ice nucleation efficiency with aging time possibly due to a change in the protonation state of the surface.

The results presented here have implications on our understanding of the direct and indirect effect of dust on climate forcing. Dust radiative forcing can be positive (heating) or negative (cooling) depending on the values of key variables that include height of dust layer, particle size, and aerosol optical depth.[2] The ability of acid-processed mineral dust particles to catalyze polycatechol formation leads to absorbance of light over a wide range of wavelengths given its dark color. Hence, this aging chemistry may change the radiative forcing by dust aerosol from negative to positive, similar to that of black carbon.

ASSOCIATED CONTENT

Supporting Information

The Supporting Information is available free of charge at https://pubs.acs.org/doi/10.1021/acsearthspacechem.0c00107.

Figures and tables showing data analysis (PDF)

AUTHOR INFORMATION

Corresponding Author

Hind A. Al-Abadleh − *Department of Chemistry and Biochemistry, Wilfrid Laurier University, Waterloo, Ontario N2L 3C5, Canada;* orcid.org/0000-0002-9425-0646; Phone: (519)884-0710, ext.2873; Email: halabadleh@wlu.ca; Fax: (519)746-0677

Authors

Nicole Link − *Department of Chemistry, University of British Columbia, Vancouver, British Columbia V6T 1Z1, Canada*

Nicole Removski − *Department of Chemistry, University of British Columbia, Vancouver, British Columbia V6T 1Z1, Canada*

Jingwei Yun − *Department of Chemistry, University of British Columbia, Vancouver, British Columbia V6T 1Z1, Canada;* orcid.org/0000-0002-7352-6754

Lauren T. Fleming − *Department of Chemistry, University of California, Irvine, California 92697, United States*

Sergey A. Nizkorodov − *Department of Chemistry, University of California, Irvine, California 92697, United States;* orcid.org/0000-0003-0891-0052

https://dx.doi.org/10.1021/acsearthspacechem.0c00107
ACS Earth Space Chem. 2020, 4, 1127−1139

Allan K. Bertram − *Department of Chemistry, University of British Columbia, Vancouver, British Columbia V6T 1Z1, Canada;* orcid.org/0000-0002-5621-2323

Complete contact information is available at: https://pubs.acs.org/10.1021/acsearthspacechem.0c00107

Author Contributions

The study was conceived by H.A.A., A.K.B., and S.A.N. N.L., N.R., and J.Y. carried out the ice nucleation measurements. L.T.F. did the MALDI measurements. All authors contributed to writing the manuscript.

Notes

The authors declare no competing financial interest.

■ ACKNOWLEDGMENTS

H.A.A. acknowledges funding from NSERC Discovery Program and the Fulbright Canada Research Chair in Atmospheric Chemistry, Air Quality, and Climate Change program at the University of California, Irvine. S.N. acknowledges support from United States NSF Grant AGS-1853639. The authors thank Dr. Md. Aminur Rahman for the BET surface area measurements, Anita Lam for the XRD analysis to determine the composition of AZTD, Ben Katz at the UCI Mass Spectrometry Facility for training and assistance with the MALDI-TOF, and Gena Braun at the Centre for Cold Regions and Water Science at Laurier for the dissolved iron analysis. The electron microscopy research described in this paper was performed at the Canadian Centre for Electron Microscopy at McMaster University, which is supported by NSERC and other government agencies.

■ REFERENCES

(1) Tang, M.; Cziczo, D. J.; Grassian, V. H. Interactions of water with mineral dust aerosol: Water adsorption, hygroscopicity, cloud condensation, and ice nucleation. *Chem. Rev.* **2016**, *116*, 4205−4259.

(2) Choobari, O. A.; Zawar-Reza, P.; Sturman, A. The global distribution of mineral dust and its impacts on the climate system: A review. *Atmos. Res.* **2014**, *138*, 152−165.

(3) Schepanski, K. Transport of mineral dust and its impact on climate. *Geosciences* **2018**, *8*, 151.

(4) Rubasinghege, G.; Elzey, S.; Baltrusaitis, J.; Jayaweera, P. M.; Grassian, V. H. Reactions on atmospheric dust particles: Surface photochemistry and size-dependent nanoscale redox chemistry. *J. Phys. Chem. Lett.* **2010**, *1*, 1729−1737.

(5) Cwiertny, D. M.; Young, M. A.; Grassian, V. H. Chemistry and photochemistry of mineral dust aerosol. *Annu. Rev. Phys. Chem.* **2008**, *59*, 27−51.

(6) Usher, C. R.; Michel, A. E.; Grassian, V. H. Reactions on mineral dust. *Chem. Rev.* **2003**, *103*, 4883−4940.

(7) Sullivan, R. C.; Guazzotti, S. A.; Sodeman, D. A.; Prather, K. A. Direct observations of the atmospheric processing of Asian mineral dust. *Atmos. Chem. Phys.* **2007**, *7*, 1213−1236.

(8) Li, W.; Shao, L.; Zhang, D.; Ro, C.-U.; Hu, M.; Bi, X.; Geng, H.; Matsuki, A.; Niu, H.; Chen, J. A review of single aerosol particle studies in the atmosphere of East Asia: Morphology, mixing state, source, and heterogeneous reactions. *J. Cleaner Prod.* **2016**, *112*, 1330−1349.

(9) Li, W.; Shao, L.; Shi, Z.; Chen, J.; Yang, L.; Yuan, Q.; Yan, C.; Zhang, X.; Wang, Y.; Sun, J.; Zhang, Y.; Shen, X.; Wang, Z.; Wang, W. Mixing state and hygroscopicity of dust and haze particles before leaving Asian continent. *J. Geophys. Res. Atmos.* **2014**, *119*, 1044−1059.

(10) Weinzierl, B.; Ansmann, A.; Prospero, J. M.; Althausen, D.; Benker, N.; Chouza, F.; Dollner, M.; Farrell, D.; Fomba, W. K.; Freudenthaler, V.; Gasteiger, J.; Groß, S.; Haarig, M.; Heinold, B.; Kandler, K.; Kristensen, T. B.; Mayol-Bracero, O. L.; Muller, T.; Reitebuch, O.; Sauer, D.; Schafler, A.; Schepanski, K.; Spanu, A.; Tegen, I.; Toledano, C.; Walser, A. The Saharan aerosol long-range transport and aerosol-cloud-interaction experiment overview and selected highlights. *Bull. Am. Meteorol. Soc.* **2017**, *98*, 1427−1451.

(11) Liu, D.; Taylor, J. W.; Crosier, J.; Marsden, N.; Bower, K. N.; Lloyd, G.; Ryder, C. L.; Brooke, J. K.; Cotton, R.; Marenco, F.; Blyth, A.; Cui, Z.; Estelles, V.; Gallagher, M.; Coe, H.; Choularton, T. W. Aircraft and ground measurements of dust aerosols over the west African coast in summer 2015 during ICE-D and AER-D. *Atmos. Chem. Phys.* **2018**, *18*, 3817−3838.

(12) Denjean, C.; Formenti, P.; Desboeufs, K.; Chevaillier, S.; Triquet, S.; Maille, M.; Cazaunau, M.; Laurent, B.; Mayol-Bracero, O. L.; Vallejo, P.; Quinones, M.; Gutierrez-Molina, I. E.; Cassola, F.; Prati, P.; Andrews, E.; Ogren, J. Size distribution and optical properties of African mineral dust after intercontinental transport. *J. Geophys. Res-Atmos.* **2016**, *121*, 7117−7138.

(13) Kadar, E.; Fisher, A.; Stolpe, B.; Calabrese, S.; Lead, J.; Valsami-Jones, E.; Shi, Z. Colloidal stability of nanoparticles derived from simulated cloud-processed mineral dusts. *Sci. Total Environ.* **2014**, *466−467*, 864−870.

(14) Riemer, N.; Ault, A. P.; West, M.; Craig, R. L.; Curtis, J. H. Aerosol mixing state: Measurements, modeling, and impacts. *Rev. Geophys.* **2019**, *57*, 187−249.

(15) Tang, M.; Huang, X.; Lu, K.; Ge, M.; Li, Y.; Cheng, P.; Zhu, T.; Ding, A.; Zhang, Y.; Gligorovski, S.; Song, W.; Ding, X.; Bi, X.; Wang, X. Heterogeneous reactions of mineral dust aerosol: Implications for tropospheric oxidation capacity. *Atmos. Chem. Phys.* **2017**, *17*, 11727−11777.

(16) Romanias, M. N.; Ourrad, H.; Thevenet, F.; Riffault, V. Investigating the heterogeneous interaction of VOCs with natural atmospheric particles: Adsorption of limonene and toluene on Saharan mineral dusts. *J. Phys. Chem. A* **2016**, *120*, 1197−1212.

(17) Chen, H.; Navea, J. G.; Young, M. A.; Grassian, V. H. Heterogeneous photochemistry of trace atmospheric gases with components of mineral dust aerosol. *J. Phys. Chem. A* **2011**, *115*, 490−499.

(18) Hoose, C.; Mohler, O. Heterogeneous ice nucleation on atmospheric aerosols: A review of results from laboratory experiments. *Atmos. Chem. Phys.* **2012**, *12*, 9817−9854.

(19) Kanji, Z. A.; Ladino, L. A.; Wex, H.; Boose, Y.; Burkert-Kohn, M.; Cziczo, D. J.; Kramer, M. Overview of ice nucleating particles. *Meteoro. Monographs* **2017**, *58*, 1.1−1.33.

(20) Sullivan, R. C.; Minambres, L.; DeMott, P. J.; Prenni, A. J.; Carrico, C. M.; Levin, E. J. T.; Kreidenweis, S. M. Chemical processing does not always impair heterogeneous ice nucleation of mineral dust particles. *Geophys. Res. Lett.* **2010**, *37*, L24805.

(21) Cziczo, D. J.; Froyd, K. D.; Gallavardin, S. J.; Moehler, O.; Benz, S.; Saathoff, H.; Murphy, D. M. Deactivation of ice nuclei due to atmospherically relevant surface coatings. *Environ. Res. Lett.* **2009**, *4*, 044013.

(22) Sullivan, R. C.; Petters, M. D.; DeMott, P. J.; Kreidenweis, S. M.; Wex, H.; Niedermeier, D.; Hartmann, S.; Clauss, T.; Stratmann, F.; Reitz, P.; Schneider, J.; Sierau, B. Irreversible loss of ice nucleation active sites in mineral dust particles caused by sulphuric acid condensation. *Atmos. Chem. Phys.* **2010**, *10*, 11471−11487.

(23) Niedermeier, D.; Hartmann, S.; Clauss, T.; Wex, H.; Kiselev, A.; Sullivan, R. C.; DeMott, P. J.; Petters, M. D.; Reitz, P.; Schneider, J.; Mikhailov, E.; Sierau, B.; Stetzer, O.; Reimann, B.; Bundke, U.; Shaw, R. A.; Buchholz, A.; Mentel, T. F.; Stratmann, F. Experimental study of the role of physicochemical surface processing on the in ability of mineral dust particles. *Atmos. Chem. Phys.* **2011**, *11*, 11131−11144.

(24) Whale, T. F.; Holden, M. A.; Wilson, T. W.; O'Sullivan, D.; Murray, B. J. The enhancement and suppression of immersion mode heterogeneous ice-nucleation by solutes. *Chem. Sci.* **2018**, *9*, 4142−4151.

(25) Niedermeier, D.; Hartmann, S.; Shaw, R. A.; Covert, D.; Mentel, T. F.; Schneider, J.; Poulain, L.; Reitz, P.; Spindler, G.;

Clauss, T.; Kiselev, A.; Hallbauer, E.; Wex, H.; Mildenberger, K.; Stratmann, F. Heterogeneous freezing of droplets with immersed mineral dust particles - measurements and parameterization. *Atmos. Chem. Phys.* **2010**, *10*, 3601−3614.
(26) Perkins, R. J.; Gillette, S. M.; Hill, T. C. J.; DeMott, P. J. The labile nature of ice nucleation by arizona test dust. *ACS Earth Space Chem.* **2020**, *4*, 133−141.
(27) Kanji, Z. A.; Sullivan, R. C.; Niemand, M.; DeMott, P. J.; Prenni, A. J.; Chou, C.; Saathoff, H.; Mohler, O. Heterogeneous ice nucleation properties of natural desert dust particles coated with a surrogate of secondary organic aerosol. *Atmos. Chem. Phys.* **2019**, *19*, 5091−5110.
(28) Satheesh, S.; Krishnamoorthy, K. Radiative effects of natural aerosols: A review. *Atmos. Environ.* **2005**, *39*, 2089−2110.
(29) Kaufman, Y. J.; Tanre, D.; Dubovik, O.; Karnieli, A.; Remer, L. A. Absorption of sunlight by dust as inferred from satellite and ground-based remote sensing. *Geophys. Res. Lett.* **2001**, *28*, 1479−1482.
(30) Dubovik, O.; Holben, B.; Eck, T. F.; Smirnov, A.; Kaufman, Y. J.; King, M. D.; Tanre, a.; Slutsker, I. Variability of absorption and optical properties of key aerosol types observed in worldwide locations. *J. Atmos. Sci.* **2002**, *59*, 590−608.
(31) Clarke, A. D.; Shinozuka, Y.; Kapustin, V. N.; Howell, S.; Huebert, B.; Doherty, S.; Anderson, T.; Covert, D.; Abderson, J.; Hua, X.; Moore, K. G., II; McNaughton, C.; Carmichael, G.; Weber, R. Size distributions and mixtures of dust and black carbon aerosol in Asian outflow: Physiochemistry and optical properties. *J. Geophys. Res.* **2004**, *109* (D15), D15S09.
(32) Scarnato, B. V.; China, S.; Nielsen, K.; Mazzoleni, C. Perturbations of the optical properties of mineral dust particles by mixing with black carbon: A numerical simulation study. *Atmos. Chem. Phys.* **2015**, *15*, 6913−6928.
(33) Liao, H.; Seinfeld, J. H. Radiative forcing by mineral dust aerosols: Sensitivity to key variables. *J. Geophys. Res. D* **1998**, *103* (D24), 31637−31645.
(34) Maher, B. A.; Prospero, J. M.; Mackie, D.; Gaiero, D.; Hesse, P. P.; Balkanski, Y. Global connections between aeolian dust, climate and ocean biogeochemistry at the present day and at the last glacial maximum. *Earth-Sci. Rev.* **2010**, *99*, 61−97.
(35) Mahowald, N.; Baker, A. R.; Bergametti, G.; Brooks, N.; Duce, R. A.; Jickells, T. D.; Kubilay, N.; Prospero, J. M.; Tegen, I. Atmospheric global dust cycle and iron inputs to the ocean. *Global Biogeochem. Cycles* **2005**, *19* (1−15), GB4025.
(36) Conway, T. M.; John, S. G. Quantification of dissolved iron sources to the north atlantic ocean. *Nature* **2014**, *511*, 212−215.
(37) Sedwick, P. N.; Sholkovitz, E. R.; Church, T. M. Impact of anthropogenic combustion emissions on the fractional solubility of aerosol iron: Evidence from the Sargasso sea. *Geochem., Geophys., Geosyst.* **2007**, *8*, Q10Q06.
(38) Guieu, C.; Bonnet, S.; Wagener, T.; Loye-Pilot, M.-D. Biomass burning as a source of dissolved iron to the open ocean? *Geophys. Res. Lett.* **2005**, *32*, L19608.
(39) Ito, A. Atmospheric processing of combustion aerosols as a source of bioavailable iron. *Environ. Sci. Technol. Lett.* **2015**, *2*, 70−75.
(40) Schulz, M.; Prospero, J. M.; Baker, A. R.; Dentener, F.; Ickes, L.; Liss, P. S.; Mahowald, N.; Nickovic, S.; Garcia-Pando, C. P.; Rodriguez, S.; Sarin, M.; Tegen, I.; Duce, R. A. Atmospheric transport and deposition of mineral dust to the ocean: Implications for research needs. *Environ. Sci. Technol.* **2012**, *46*, 10390−10404.
(41) Ito, A.; Shi, Z. Delivery of anthropogenic bioavailable iron from mineral dust and combustion aerosols to the ocean. *Atmos. Chem. Phys.* **2016**, *16*, 85−99.
(42) Ito, A.; Myriokefalitakis, S.; Kanakidou, M.; Mahowald, N.; Scanza, R. A.; Hamilton, D. S.; Baker, A. R.; Jickells, T. D.; Sarin, M.; Bikkina, S.; Gao, Y.; Shelley, R. U.; Buck, C. S.; Landing, W. M.; Bowie, A. R.; Perron, M. M. G.; Guieu, C.; Meskhidze, N.; Johnson, M. S.; Feng, Y.; Kok, J. F.; Nenes, A.; Duce, R. A. Pyrogenic iron: The missing link to high iron solubility in aerosols. *Sci. Adv.* **2019**, *5*, No. eaau7671.
(43) Oakes, M.; Weber, R. J.; Lai, B.; Russell, A.; Ingall, E. D. Characterization of iron speciation in urban and rural single particles using XANES spectroscopy and micro x-ray fluorescence measurements: Investigating the relationship between speciation and fractional iron solubility. *Atmos. Chem. Phys.* **2012**, *12*, 745−756.
(44) Butler, A. J.; Andrew, M. S.; Russell, A. G. Daily sampling of PM2.5 in Atlanta: Results of the first year of the assessment of spatial aerosol composition in Atlanta study. *J. Geophys. Res.* **2003**, *108*, SOS 3−1−SOS 3−11.
(45) Hoffmann, P.; Dedik, A. N.; Ensling, J.; Weinbruch, S.; Weber, S.; Sinner, T.; Gutlich, P.; Ortner, H. M. Speciation of iron in atmospheric aerosol samples. *J. Aerosol Sci.* **1996**, *27*, 325−327.
(46) Johansen, A. M.; Siefert, R.; Hoffmann, M. R. Chemical composition of aerosols collected over the tropical north Atlantic ocean. *J. Geophys. Res-Atmos.* **2000**, *105*, 15277−15312.
(47) Liu, W.; Wang, Y. H.; Russell, A.; Edgerton, E. S. Atmospheric aerosol over two urban-rural pairs in the southeastern United States: Chemical composition and possible sources. *Atmos. Environ.* **2005**, *39*, 4453−4470.
(48) Oakes, M.; Rastogi, N.; Majestic, B. J.; Shafer, M.; Schauer, J. J.; Edgerton, E. S.; Weber, R. J. Characterization of soluble iron in urban aerosols using near-real time data. *J. Geophys. Res.* **2010**, *115*, 1−12.
(49) Ault, A. P.; Peters, T. M.; Sawvel, E. J.; Casuccio, G. S.; Willis, R. D.; Norris, G. A.; Grassian, V. H. Single-particle SEM-EDX analysis of iron-containing coarse particulate matter in an urban environment: Sources and distribution of iron within Cleveland, Ohio. *Environ. Sci. Technol.* **2012**, *46*, 4331−4339.
(50) Guasco, T. L.; Cuadra-Rodriguez, L. A.; Pedler, B. E.; Ault, A. P.; Collins, D. B.; Zhao, D.; Kim, M. J.; Ruppel, M. J.; Wilson, S. C.; Pomeroy, R. S.; Grassian, V. H.; Azam, F.; Bertram, T. H.; Prather, K. A. Transition metal associations with primary biological particles in sea spray aerosol generated in a wave channel. *Environ. Sci. Technol.* **2014**, *48*, 1324−1333.
(51) Ault, A. P.; Moore, M. J.; Furutani, H.; Prather, K. A. Impact of emissions from the Los Angeles port region on San Diego air quality during regional transport events. *Environ. Sci. Technol.* **2009**, *43*, 3500−3506.
(52) Ault, A. P.; Gaston, C. J.; Wang, Y.; Dominguez, G.; Thiemens, M. H.; Prather, K. A. Characterization of the single particle mixing state of individual ship plume events measured at the port of Los Angeles. *Environ. Sci. Technol.* **2010**, *44*, 1954−1961.
(53) Deboudt, K.; Flament, P.; Choel, M.; Gloter, A.; Sobanska, S.; Colliex, C. Mixing state of aerosols and direct observation of carbonaceous and marine coatings on African dust by individual particle analysis. *J. Geophys. Res-Atmos.* **2010**, *115*, D24207.
(54) Takahama, S.; Gilardoni, S.; Russell, L. M. Single-particle oxidation state and morphology of atmospheric iron aerosols. *J. Geophys. Res.* **2008**, *113*, D22202.
(55) Oppo, C.; Bellandi, S.; Innocenti, N. D.; Stortini, A. M.; Loglio, G.; Schiavuta, E.; Cini, R. Surfactant components of marine organic matter as agents for biogeochemical fractionation and pollutant transport via marine aerosols. *Mar. Chem.* **1999**, *63*, 235−253.
(56) Piotrowicz, S. R.; Duce, R. A.; Fasching, J. L.; Weisel, C. P. Bursting bubbles and their effect on the sea-to-air transport of Fe, Cu and Zn. *Mar. Chem.* **1979**, *7*, 307−324.
(57) Weisel, C. P.; Duce, R. A.; Fasching, J. L.; Heaton, R. W. Estimates of the transport of trace-metals from the ocean to the atmosphere. *J. Geophys. Res.* **1984**, *89*, 11607.
(58) Shi, Z. B.; Krom, M. D.; Jickells, T. D.; Bonneville, S.; Carslaw, K. S.; Mihalopoulos, N.; Baker, A. R.; Benning, L. G. Impacts on iron solubility in the mineral dust by processes in the source region and the atmosphere: A review. *Aeolian Res.* **2012**, *5*, 21−42.
(59) McDaniel, M. F. M.; Ingall, E. D.; Morton, P. L.; Castorina, E.; Weber, R. J.; Shelley, R. U.; Landing, W. M.; Longo, A. F.; Feng, Y.; Lai, B. Relationship between atmospheric aerosol mineral surface area and iron solubility. *ACS Earth Space Chem.* **2019**, *3*, 2443−2451.
(60) Paris, R.; Desboeufs, K.; Formenti, P.; Nava, S.; Chou, C. Chemical characterisation of iron in dust and biomass burning

https://dx.doi.org/10.1021/acsearthspacechem.0c00107
ACS Earth Space Chem. 2020, 4, 1127−1139

aerosols during AMMA-SOP0/DABEX: Implication for iron solubility. *Atmos. Chem. Phys.* **2010**, *10*, 4273−4282.
(61) Benner, R. Loose ligands and available iron in the ocean. *Proc. Natl. Acad. Sci. U. S. A.* **2011**, *108*, 893−894.
(62) Boyd, P. W.; Ellwood, M. J. The biogeochemical cycle of iron in the ocean. *Nat. Geosci.* **2010**, *3*, 675−682.
(63) Schroth, A. W.; Crusius, J.; Sholkovitz, E. R.; Bostick, B. C. Iron solubility driven by speciation in dust sources to the ocean. *Nat. Geosci.* **2009**, *2*, 337−340.
(64) Chen, H.; Grassian, V. H. Iron dissolution of dust source materials during simulated acidic processing: The effect of sulfuric, acetic, and oxalic acids. *Environ. Sci. Technol.* **2013**, *47*, 10312−10321.
(65) Rubasinghege, G.; Lentz, R. W.; Scherer, M. M.; Grassian, V. H. Simulated atmospheric processing of iron oxyhydroxide minerals at low pH: Roles of particle size and acid anion in iron dissolution. *Proc. Natl. Acad. Sci. U. S. A.* **2010**, *107*, 6628−6633.
(66) Chen, H.; Laskin, A.; Baltrusaitis, J.; Gorski, C. A.; Scherer, M. M.; Grassian, V. H. Coal fly ash as a source of iron in atmospheric dust. *Environ. Sci. Technol.* **2012**, *46*, 2112−2120.
(67) Buck, C. S.; Landing, W. M.; Resing, J. A. Particle size and aerosol iron solubility: A high-resolution analysis of Atlantic aerosols. *Mar. Chem.* **2010**, *120*, 14−24.
(68) Meskhidze, N.; Hurley, D.; Royalty, T. M.; Johnson, M. S. Potential effect of atmospheric dissolved organic carbon on the iron solubility in seawater. *Mar. Chem.* **2017**, *194*, 124−132.
(69) Paris, R.; Desboeufs, K. Effect of atmospheric organic complexation on iron-bearing dust solubility. *Atmos. Chem. Phys.* **2013**, *13*, 4895−4905.
(70) Wozniak, A. S.; Shelley, R. U.; McElhenie, S. D.; Landing, W. M.; Hatcher, P. G., Aerosol water soluble organic matter characteristics over the north atlantic ocean: Implications for iron-binding ligands and iron solubility. *Mar. Chem.* **2015***173*, 162−172.
(71) Fang, T.; Guo, H.; Zeng, L.; Verma, V.; Nenes, A.; Weber, R. J. Highly acidic ambient particles, soluble metals, and oxidative potential: A link between sulfate and aerosol toxicity. *Environ. Sci. Technol.* **2017**, *51*, 2611−2620.
(72) Gonzalez, M. C.; Roman, E. S. Environmental photochemistry in heterogeneous media. In *Hdb environmental chemistry*; Springer-Verlag: Berlin, 2005; Vol. *2*, pp 49−75.
(73) Al-Abadleh, H. A. A review on the bulk and surface chemistry of iron in atmospherically-relevant systems containing humic like substances. *RSC Adv.* **2015**, *5*, 45785−45811.
(74) George, C.; D'Anna, B.; Herrmann, H.; Weller, C.; Vaida, V.; Donaldson, D. J.; Bartels-Rausch, T.; Ammann, M. Emerging areas in atmospheric photochemistry. In *Atmospheric and aerosol chemistry*; McNeill, V. F., Ariya, P. A., Eds.; Springer: Heidelberg, 2012; Vol. *339*, pp 1−54.
(75) Shi, Z.; Krom, M. D.; Bonneville, S.; Benning, L. G. Atmospheric processing outside clouds increases soluble iron in mineral dust. *Environ. Sci. Technol.* **2015**, *49*, 1472−1477.
(76) Stumm, W. *Chemistry of the solid-water interface*; John Wiley & Sons, Inc.: New York, 1992.
(77) Charrier, J. G.; Anastasio, C. On dithiothreitol (DTT) as a measure of oxidative potential for ambient particles: Evidence for the importance of soluble transition metals. *Atmos. Chem. Phys.* **2012**, *12*, 9321−9333.
(78) Huang, L.; Cochran, R. E.; Coddens, E. M.; Grassian, V. H. Formation of organosulfur compounds through transition metal ion-catalyzed aqueous phase reactions. *Environ. Sci. Technol. Lett.* **2018**, *5*, 315−321.
(79) Slikboer, S.; Grandy, L.; Blair, S. L.; Nizkorodov, S. A.; Smith, R. W.; Al-Abadleh, H. A. Formation of light absorbing soluble secondary organics and insoluble polymeric particles from the dark reaction of catechol and guaiacol with Fe(III). *Environ. Sci. Technol.* **2015**, *49*, 7793−7801.
(80) Tran, A.; Williams, G.; Younus, S.; Ali, N. N.; Blair, S. L.; Nizkorodov, S. A.; Al-Abadleh, H. A. Efficient formation of light-absorbing polymeric nanoparticles from the reaction of soluble Fe(III) with C4 and C6 dicarboxylic acids. *Environ. Sci. Technol.* **2017**, *51*, 9700−9708.
(81) Al Nimer, A.; Rocha, L.; Rahman, M. A.; Nizkorodov, S. A.; Al-Abadleh, H. A. Effect of oxalate and sulfate on iron-catalyzed secondary brown carbon formation. *Environ. Sci. Technol.* **2019**, *53*, 6708−6717.
(82) Lavi, A.; Lin, P.; Bhaduri, B.; Carmieli, R.; Laskin, A.; Rudich, Y. Characterization of light-absorbing oligomers from reactions of phenolic compounds and Fe(III). *ACS Earth Space Chem.* **2017**, *1*, 637−646.
(83) Laskin, A.; Laskin, J.; Nizkorodov, S. A. Chemistry of atmospheric brown carbon. *Chem. Rev.* **2015**, *115*, 4335−4382.
(84) Rahman, M. A.; Al-Abadleh, H. A. Surface water structure and hygroscopic properties of light absorbing secondary organic polymers of atmospheric relevance. *ACS Omega* **2018**, *3*, 15519−15529.
(85) Method 200.2, revision 2.8: Sample preparation procedure for spectrochemical determination of total recoverable elements. https://www.epa.gov/sites/production/files/2015-08/documents/method_200-2_rev_2-8_1994.pdf (accessed June 5, 2020).
(86) DeMott, P. J.; Mason, R. H.; McCluskey, C. S.; Hill, T. C. J.; Perkins, R. J.; Desyaterik, Y.; Bertram, A. K.; Trueblood, J. V.; Grassian, V. H.; Qiu, Y.; Molinero, V.; Tobo, Y.; Sultana, C. M.; Lee, C.; Prather, K. A. Ice nucleation by particles containing long-chain fatty acids of relevance to freezing by sea spray. *Environ. Sci.: Processes Impacts* **2018**, *20*, 1559−1569.
(87) Gruendling, T.; Weidner, S.; Falkenhagen, J.; Barner-Kowollik, C. Mass spectrometry in polymer chemistry: A state-of-the-art update. *Polym. Chem.* **2010**, *1*, 599−617.
(88) Meskhidze, N.; Volker, C.; Al-Abadleh, H. A.; Barbeau, K.; Bressac, M.; Buck, C.; Bundy, R. M.; Croot, P. L.; Feng, Y.; Ito, A.; Johansen, A. M.; Landing, W. M.; Mao, J.; Myriokefalitakis, S.; Ohnemus, D.; Pasquier, B.; Ye, Y. Perspective on identifying and characterizing the processes controlling iron speciation and residence time at the atmosphere-ocean interface. *Mar. Chem.* **2019**, *217* (1−16), 103704.
(89) Chernyshova, I. V.; Ponnurangam, S.; Somasundaran, P. Linking interfacial chemistry of CO_2 to surface structures of hydrated metal oxide nanoparticles: Hematite. *Phys. Chem. Chem. Phys.* **2013**, *15*, 6953−6964.
(90) Lanzl, C. A.; Baltrusaitis, J.; Cwiertny, D. M. Dissolution of hematite nanoparticle aggregates: Influence of primary particle size, dissolution mechanism, and solution pH. *Langmuir* **2012**, *28*, 15797−15808.
(91) Gulley-Stahl, H.; Hogan, P. A., II; Schmidt, W. L.; Wall, S. J.; Buhrlage, A.; Bullen, H. A. Surface complexation of catechol to metal oxides: An ATR-FTIR adsorption and dissolution study. *Environ. Sci. Technol.* **2010**, *44*, 4116−4121.
(92) Situm, A.; Rahman, M. A.; Goldberg, S.; Al-Abadleh, H. A. Spectral characterization and surface complexation modeling of organics on hematite nanoparticles: Role of electrolytes in the binding mechanism. *Environ. Sci.: Nano* **2016**, *3*, 910−926.
(93) Johnson, S. B.; Yoon, T. H.; Kocar, B. D.; Brown, G. E., Jr. Adsorption of organic matter at mineral/water interfaces. Outersphere adsorption of maleate and implications for dissolution processes. *Langmuir* **2004**, *20*, 4996−5006.
(94) Bondietti, G.; Sinniger, J.; Stumm, W. III. The reactivity of Fe(III) (hydr)oxides: Effects of ligands in inhibiting the dissolution. *Colloids Surf., A* **1993**, *79*, 157−167.
(95) Hug, S. J. In situ fourier transform infrared measurements of sulfate adsorption on hematite in aqueous solutions. *J. Colloid Interface Sci.* **1997**, *188*, 415−422.
(96) Colarieti, M. L.; Toscano, G.; Ardi, M. R.; Greco, G., Jr. Abiotic oxidation of catechol by soil metal oxides. *J. Hazard. Mater.* **2006**, *134*, 161−168.
(97) Larson, R. A.; Hufnal, J. M., Jr. Oxidative polymerization of dissolved phenols by soluble and insoluble inorganic species. *Limnol. Oceanogr.* **1980**, *25*, 505−512.
(98) Seinfeld, J. H.; Pandis, S. N. *Atmospheric chemistry and physics: From air pollution to climate change*; Wiley: New York, 2006.

(99) Pillar, E. A.; Zhou, R.; Guzman, M. I. Heterogeneous oxidation of catechol. *J. Phys. Chem. A* **2015**, *119*, 10349−10359.
(100) Kosmulski, M. Isoelectric points and points of zero charge of metal (hydr)oxides: 50 years after parks' review. *Adv. Colloid Interface Sci.* **2016**, *238*, 1−61.
(101) Abdelmonem, A. Direct molecular-level characterization of different heterogeneous freezing modes on mica - part 1. *Atmos. Chem. Phys.* **2017**, *17*, 10733−10741.
(102) Kumar, A.; Marcolli, C.; Luo, B.; Peter, T. Ice nucleation activity of silicates and aluminosilicates in pure water and aqueous solutions - part 1: The k-feldspar microcline. *Atmos. Chem. Phys.* **2018**, *18*, 7057−7079.
(103) Kumar, A.; Marcolli, C.; Peter, T. Ice nucleation activity of silicates and aluminosilicates in pure water and aqueous solutions - part 2: Quartz and amorphous silica. *Atmos. Chem. Phys.* **2019**, *19*, 6035−6058.

https://dx.doi.org/10.1021/acsearthspacechem.0c00107
ACS Earth Space Chem. 2020, 4, 1127−1139